Biotribology 18 (2019) 100093

Contents lists available at ScienceDirect

Biotribology

journal homepage: www.elsevier.com/locate/biotri

Fretting-corrosion of cardiovascular stent materials: The role of electrochemical polarisation on debris generation mechanisms

Emily R. Clark[a,b], Karen E. Porter[b], Michael G. Bryant[a,*]

[a] Institute of Functional Surfaces, School of Mechanical Engineering, University of Leeds, Leeds, UK
[b] Leeds Institute for Cardiovascular and Metabolic Medicine, University of Leeds, Leeds, UK

1. Introduction

Balloon angioplasty and implantation of stents has been used as a successful intervention for atherosclerosis for upwards of 40 years, yet clinical limitations persist. In-stent restenosis (ISR) accounts for about 10% of coronary stent failures, increasing to 30% in peripheral stents, 1 year post-implantation in the modern stent era requiring further intervention [1,2]. In-stent restenosis (ISR) is characterised by a re-narrowing of the artery post-stent implantation to such an extent that blood flow is hindered to the downstream organ [3]. The principle cellular component of the arterial wall are smooth muscle cells (SMCs) which migrate towards the lumen of the artery, proliferate and secrete extracellular matrix components during development of ISR [4]. The advent of drug-eluting stents (DES) has gone some way to reducing the incidence of ISR but the issue remains in a non-negligible patient subset [5]. In contrast with the clinical post-failure analysis conducted in orthopaedic implants, stents with ISR are typically not removed from the patient: re-stenting or bypass grafts are used [6,7]. Post-failure inspection and analysis of the devices is therefore hampered and the true occurrence of fretting and corrosion in-vivo is unknown.

The surfaces and interfaces established during the implantation of a vascular devices are receiving increased scrutiny due to the possible adverse soft tissue effects associated with implant derived debris. Surface analysis of retrieved vascular devices has demonstrated that interfaces are susceptible to fretting-corrosion; the combined action of mechanical wear and corrosion at small displacement amplitudes. Evidence of fretting-corrosion has been observed at the braided stent strut interface [7,8] and in vivo at overlapping interfaces were the use of multiple stents may be necessary to treat long lesions and those arising from complex and dynamic biomechanics, particularly in peripheral stents [6,7,9]. Such interfaces are shown in Fig. 1. Within the vasculature, stenting undergoes large deformations through haemostatic forces (e.g. pulsatile flow, pressure) and daily-living activities (e.g., leg flexion) introducing micro-displacements at overlapping or braided interfaces. Previous studies [10,11] have shown that overlapping and braided stents (Fig. 1a) exhibit evidence of wear and corrosion after laboratory simulation. This is supported by in-vivo observations [12,13] (Fig. 1b), in which a tentative link between metallic degradation, inflammation and ISR has been hypothesised. Therefore it is conceivable that the nature of micro-motion and contact conditions at the interface can be incredibly transient and activity dependant.

Degradation products (metal ions and nano-particles) arising from the fretting-corrosion interfaces will be released into the circulation and local tissues depending upon the degree of re-endothelialisation. Metallic debris arising from cardiovascular devices, in the form of metallic ions or bulk metal particles, has been shown to have a biological effect on cells and tissue and can mediate oxidative stress, release of proinflammatory mediators, cytotoxicity, DNA damage and functional cellular changes such as proliferation [14–17]. These same biological effects are also implicated in the pathogenesis of in-stent restenosis [1,4]. To elucidate the links between device degradation and adverse biological processes, some studies have used sources such as metal chloride salts [15,18,19], passive corrosion through incubation under physiological conditions [20–22] or application of an electrical potential to simulate and accelerate the oxidising action of the physiological corrosive environment [16,20]. The role of tribocorrosion products (i.e. metal ions and particles) on vascular biology processes are yet to be fully considered. It is also well known that the characteristics (e.g. chemistry, thickness, stoichiometry, formation kinetics) of the passive layer on the surface of biomedical alloys, such as CoCrMo and NiTi, is dependent upon the applied potential in corrosion systems [23,24] and influences the synergistic electrochemical and mechanical degradation of a metallic alloy [25–28].

In order to accurately assess the biological responses to metallic debris, the pathways to their production must be fully considered, particular when qualifying materials and devices pre-clinically. In a comprehensive review Mischler found that the potentiostatic method, whereby the system is held at a nominal potential during fretting-corrosion, is the most commonly used tribo-electrochemical method [29]. This method has been used variously to understand the mechanisms of fretting-corrosion which are representative of implanted metallic medical devices in vivo [23,30–33]. In reality, the potential under free corrosion conditions is dynamic and evolves over time [27,34,35].

* Corresponding author at: iFS, School of Mechanical Engineering, University of Leeds, Woodhouse Lane, Leeds, West Yorkshire LS2 9JT, UK.
E-mail address: M.G.Bryant@leeds.ac.uk (M.G. Bryant).

https://doi.org/10.1016/j.biotri.2019.100093
Received 19 November 2018; Received in revised form 2 April 2019; Accepted 4 April 2019
Available online 05 April 2019

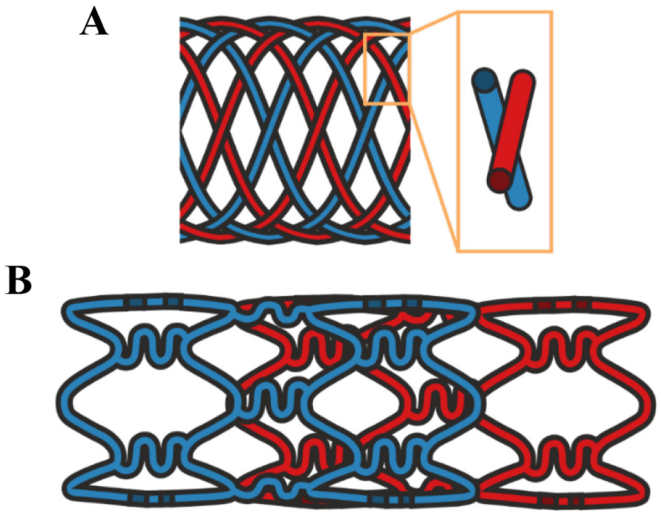

Fig. 1. Schematic of fretting-corrosion interfaces in cardiovascular stents. (A) Cross-wire interface in braided stents (shown with close up), more commonly used in peripheral arteries. (B) Laser cut type stents in an overlapping configuration, often used for long atherosclerotic lesions or re-intervention due to ISR.

Conducting fretting-corrosion tests at the free potential of the system (or open circuit potential, OCP) has therefore more recently been used to simulate the physiological fretting-corrosion mechanisms of biomaterials [36,37]. The experimental methodology to understand bio-tribocorrosion mechanisms and released wear debris can fundamentally alter the results. Differences in wear debris chemistry and morphology can instigate differential biological effects [17,38]. Questions must be raised as to the suitability of imposing electrochemical potentials to simulate corrosion in tribological contacts, its relevance to the pre-clinical assessment, its implication on the nature of degradation and correlation between imposed electrochemical polarisation and free corrosion conditions.

The aim of this study was therefore to perform a detailed tribocorrosion study investigating the effects of polarisation on generated wear debris and material degradation during fretting in a simulated stented physiological environment. Two primary metallic biomaterials were investigated, cobalt-chromium-molybdenum (widely used biomaterial) and nickel-titanium (common vascular material) were investigated in a braided stent strut model simulating the geometric considerations. The need for further detailed investigation to understand the role of tribocorrosion and electrochemical potential/current distributions in the vascular environment has been emphasised by leading cardiologists [39]. We have shown these degradation mechanisms to be detrimental to the performance of other metallic devices implanted into the biological environment [40].

2. Materials and Methods

2.1. Materials

Superelastic nickel-titanium, NiTi, (Nitinol, NDC, USA) and low carbon cobalt-chromium-molybdenum alloy, CoCrMo, (ASTM F1537, Heymark Metals, UK) was machined into cylindrical samples Ø6 mm to represent cylindrical braided stent struts. CoCrMo was for benchmarking due to our extensive experience with this alloy. Chemical composition of alloys used in this study are shown in Table 1 according to manufacturer. Prior to experimentation, all samples were polished to a surface roughness, R_a > 25 nm using a polishing cloth (Buehler, Germany) and graded diamond polishing pastes (Kemet International Ltd., Kent, UK), cleaned with acetone and air-dried.

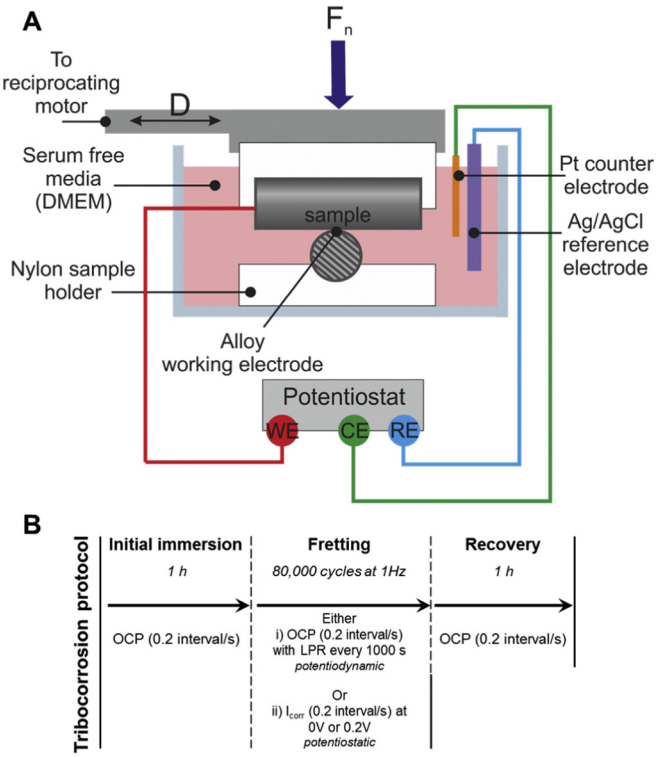

Fig. 2. (A) Experimental set-up of simulated braided stent strut fretting (perpendicular cylinder configuration). Hatching indicates cross section. (B) Protocol for fretting-corrosion testing under either potentiodynamic or potentiostatic regimes.

Serum-free culture media composed of Dulbecco's Modified Eagle Medium supplemented with 1% v/v L-glutamine (necessary growth factor) and 1% v/v antibiotic-antimycotic (Gibco, Renfrewshire, UK). This formulation is widely used in cell culture to simulate the physiological biochemical environment was used as the lubricant in this study [41,42].

2.2. Fretting Tribometer

Interactions between wear and corrosion were investigated using a custom-built reciprocating electromechanical fretting tribometer, previously developed, described and validated [43]. A schematic for the setup is shown in Fig. 2A. An electromechanical actuator provided reciprocating motion to the upper cylinder with an amplitude of 200 μm (δ_d) and was maintained at a frequency of 1 Hz, simulating that of a physiological heartbeat. δ_d = 200 μm was chosen to ensure we remain in the gross-slip regime for the duration of the test, to best represent the stent device observations (i.e. abrasion distances on the struts) [12] and FEA analysis [16]. Reciprocating motion was measured by means of a fibre optic sensor fixed in the holder mounted to the base fixture of the

Table 1
Chemical composition of low carbon CoCrMo and superelastic NiTi used in this study as stated by the manufacturer.

Element (Wt%)	Cr	Mo	Mn	Si	Ni	Fe	N	C	Co
CoCrMo	26.0–30.3	5.0–7.0	0–1.0	0–1.0	0–1.0	0–0.75	0–0.25	0–0.14	Bal
Element (Wt%)	Ni	Ti							
NiTi	55.0	45.0							

Table 2
Maximum pressure at cylinder contact as calculated by Hertzian analysis.

Alloy	Young's modulus (GPa)	Poisson's ratio	Maximum contact pressure (P_{max}) (GPa)
CoCrMo	220	0.29	0.68
NiTi	34	0.33	0.21

fretting apparatus. The tangential force (F_t) was measured throughout the experiments using a cylindrical force transducer (Kistler, USA) mounted axially to the actuator and the upper alloy cylinder. The initial normal load (F_n) at the contact between upper and lower samples was set using a force transducer (RDP Electronics, UK). A normal load of 4 N was used for each experiment (Table 2), achieving contact pressures similar to values reported by finite element analysis for overlapping cobalt-alloy stents [6]. Analysis of the fretting-loop data was done according to the criteria outlined by Fouvry et al. [44].

2.3. Fretting-corrosion Arrangement

A three electrode electrochemical cell was integrated into the fretting tribometer (Fig. 2A). The physical connection of the upper cylinder to the lower cylinder immersed in the serum-free culture media acted as the net-working electrode (WE). A combined Ag/AgCl reference electrode (RE; +0.196 V vs. standard hydrogen electrode) and Pt counter electrode (CE) (Orion, ThermoFisher Scientific, MA, US) was held in the serum-free culture media to complete the electrochemical cell. The WE, RE and CE were connected to a computer controlled potentiostat (PGSTAT101, Metrohm, Switzerland).

2.3.1. Fretting-corrosion Protocol

The protocol for the fretting-corrosion experiments is shown in Fig. 2B. Briefly, the NiTi cylinders were polished, cleaned and dried before installation into the fretting rig in a perpendicular configuration. The serum-free culture media was then added and the upper and lower cylinders were immersed in contact with each other and left for 1 h. For each condition, the OCP was recorded in this interval. Subsequently, fretting occurred for 80,000 cycles at 1 Hz for all tests. After the fretting test, the alloy was left to recover for 1 h before the tests were dismantled and the cylinders and the serum-free culture media were collected for analysis. Serum-free culture media was frozen at −20 °C to prevent dissolution of particles.

The fretting-corrosion behaviour of the simulated braided strut interface was evaluated under three conditions:

Open circuit potential (OCP) with intermittent linear polarisation resistance (LPR) measurements at which the alloy is under free corrosion conditions enabling characterisation of the interface at equilibrium. This approach has been extensively used and published in the literature for the long term assessment of tribocorrosion contacts [43,45,46]. Measurement at free corrosion potential (E_{corr}) with LPR allows quantitative in situ dynamic corrosion measurements. LPR measurements were taken every 1000 s at an applied potential of ± 0 0.02 V versus OCP at a scan rate of 0.25 mV·s^{-1}. It is widely accepted that applying such a potential no permanent changes to the electrode surface are incurred [45]. The scan rates chosen in this study are sufficiently slow enough to eliminate any capacitive charging effects due to polarisation and show no evidence of hysteresis (i.e. charging) on reversal of the potential [47]. The linear relationship between potential and current was used to calculate the polarisation resistance (R_p). This was then used in conjunction with the experimentally determined Tafel constants and the Stern-Geary (SG) relationship (Eq. (1)) [48] to determine corrosion current (I_{corr}) for the duration of the experiment. Tafel constants for cross-cylinder contact for both CoCrMo and NiTi alloys in serum-free culture media were experimentally determined under static conditions. Samples were immersed for 1 h to allow the open circuit potential (OCP) to reach equilibrium before polarisation to ± 0.6 V vs RE at a scan rate of 0.25 mV·s^{-1} to capture the Tafel regions. For each alloy, the slope of the linear anodic and cathodic regions of current in relation to overpotential (β_a and β_c respectively) were taken as the Tafel constants.

$$I_{corr} = SG\left(\frac{1}{R_p}\right) \quad (1)$$

where R_p = polarisation resistance, SG = Stern-Geary coefficient, I_{corr} = corrosion current density, and.

$$SG = \frac{\beta_a . \beta_c}{2.303\,(\beta_a + \beta_c)} \quad (2)$$

where β_a and β_c = anodic and cathodic Tafel constants respectively.

Potentiostatic polarisation was conducted at either 0 V or 0.2 V vs RE for the duration of the experiment. Tribocorrosion at increasing potentials within passive domain were selected to accelerate the anodic processes. The current transient was recorded at 5 s intervals and both potentials were below the breakdown potential of each alloy in serum-free culture medium as experimentally determined during cyclic polarisation for determination of Tafel constants.

2.4. Optical Microscopy (OM)

Optical microscopy (DM6000M, Leica, Germany) was used to inspect the wear scar and observe surface changes on both the upper and lower cylinders after fretting corrosion. As the surfaces of the cylinders were curved, a 3D montage imaging technique (*Z*-stack) was used to ensure all parts of the images were in focus.

2.5. Vertical Scanning Interferometry (VSI)

The volume loss of material from the upper and lower cylinders was determined using vertical scanning interferometry (VSI) (NPFlex, Bruker, US) with a 10× objective. Prior to VSI analysis, the cylinders were lightly cleaned using acetone to remove superficially adhered debris. The measurement area was adjusted to accommodate the varying sizes of wear scar. The volume loss was defined as the negative volume of the wear scar from the mean zero plane of the surface. The total mass loss due to both wear and corrosion mechanisms was defined as the sum of the mass loss from the upper and lower cylinders and was extrapolated from the volume loss using appropriate material density (CoCrMo: 8.4 g/cm^3; NiTi: 6.5 g/cm^3). VSI data was analysed using Vision 64 software (Bruker, MA, US). Cylindrical curvature and tilt was removed and a median data filter of magnitude 3 was applied.

2.6. Scanning Electron Microscopy (SEM)

Scanning electron microscopy with energy dispersive X-ray analysis (SEM-EDX) (Carl Zeiss EVO MA15, ZEISS, Germany) was used to determine changes in the chemical composition of the wear scar at the fretting contact. Samples were imaged with a beam intensity of 20 kV and EDX was performed at a working distance of 8 mm.

2.7. Inductively Coupled Plasma Mass Spectroscopy (ICP-MS)

Corrosion products in the media were analysed according the methods outlined by Simoes et al. [49]. Ion concentration and composition was measured with inductively coupled plasma mass spectroscopy (ICP-MS). A small volume of the serum-free culture media from the fretting tests was taken and passed through a 2 kDa ultrafilter (Vivacon, Sartorius AG, Germany) at 14,000 × g for 1 h in a centrifuge to remove all particles. The ultrafiltered media was then diluted by 100× in 2% v/v nitric acid (Fluka, Honeywell, Romania) in ultrapure water and analysed for Co, Cr, Mo, Ni and Ti isotopes using ICP-MS standards

for calibration for aforementioned elements (Sigma-Aldrich, USA). A matrix blank of serum-free media was also prepared to characterise background elemental signals from the media itself.

2.8. Particle Analysis

A volume of 1 mL of the serum free culture media used as electrolyte during the fretting experiment was defrosted and centrifuged at 14,000 × *g* for 1.5 h. The supernatant was then carefully removed and the particles were resuspended in ultrapure water to remove traces of essential salts from the serum-free culture media. The centrifugation and resuspension process was repeated 5 times per sample when the supernatant was removed leaving a pellet of particles in 250 µL of ultrapure water. The particle pellets were then sonicated for 30 mins at 37 °C. The particle suspension was then pipetted onto adhesive carbon SEM stubs and left to air dry. The particles were then imaged using SEM-EDX to analyse their morphology and chemical composition.

2.9. Statistical Analysis

A one-way ANOVA with post-hoc Tukey test was performed for each alloy (CoCrMo and NiTi) to assess the significance of impact of the polarisation regime (OCP, 0 V, 0.2 V) on total mass loss and composition of ions released to the electrolyte. A p-value of < 0.05 was considered significant for all analyses. Error bars on graphs are presented as 95% confidence intervals.

3. Results

3.1. Static Cyclic Polarisation

Fig. 3 shows the Tafel plots obtained for CoCrMo and NiTi under static conditions. The corrosion current density (I_{corr}) and free corrosion potential (E_{corr}) determined through Tafel fitting are shown in the inset of Fig. 3. Tafel constants and the associated Stern-Geary coefficient used later in the analysis of LPR data are tabulated in Table 3.

3.2. Mechanical Fretting Results

Representative fretting loops for CoCrMo and NiTi alloy ($n = 3$) under polarisation regimes at OCP and held at 0 V and 0.2 V are shown in Fig. 4. For each condition, fretting loops from intermittent cycles are shown to demonstrate the evolution of the fretting regime over time. Cumulative dissipated energy over 80,000 cycles as characterised by the mathematical area of the fretting loop is shown in Fig. 5A and B for

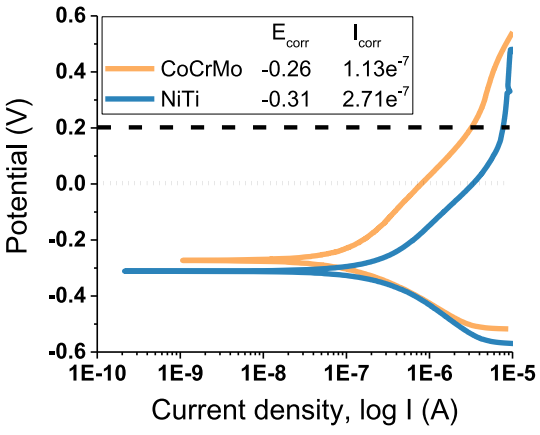

Fig. 3. Polarisation curves of CoCrMo and NiTi alloy in serum-free media. Potential range − 0.6 V to + 0.6 V with scan rate of 0.167 mV·s^{-1}. Polarisation potential for potentiostatic regime shown for 0 V (dotted line) and 0.2 V (dashed line).

Table 3
Tafel constants of CoCrMo and NiTi alloy in serum-free culture media.

Alloy	Anodic Tafel constant (β_a, V/dec)	Cathodic Tafel constant (β_c, V/dec)	Stern-Geary coefficient
CoCrMo	0.31	0.17	0.048
NiTi	0.29	0.21	0.053

CoCrMo and NiTi respectively. Representative optical microscopy and VSI images of the wear scar for CoCrMo and NiTi under all three polarisation conditions are shown in Fig. 6.

3.2.1. Fretting Loops

Under all polarisation regimes, CoCrMo alloy operated within a gross-slip regime characterised by a quasi-rectangular fretting loop with a sliding / displacement ratio, $\frac{\delta_s}{\delta_d} = 0.93 - 0.95$; well within the gross-slip criteria given by Fouvry [50]. Under fretting-corrosion at OCP, CoCrMo alloy did not demonstrate any evolution in the fretting regimes over time and the loops over the course of 80,000 cycles are relatively similar with an almost indistinguishable fretting loop area (Fig. 4A). When the polarisation potential was increased to 0 V, fretting remained in a gross-slip regime but the fretting loop area increased over time (Fig. 4B). At 0.2 V polarisation potential, CoCrMo again operated in a quasi-rectangular gross-slip regime with an increase in fretting loop area over time and was overall greater than at lower polarisation potentials (Fig. 4C). As CoCrMo existed in a gross-slip regime for OCP, 0 V and 0.2 V, increasing the polarisation potential during fretting-corrosion did not therefore appear to alter the mechanism of the fretting regime. However, polarisation to both 0 V and 0.2 V resulted in changes to the fretting loop area over time which was not present at OCP.

The fretting conditions for superelastic NiTi alloy also exhibited a gross-slip fretting regime with $\frac{\delta_s}{\delta_d}$ varying between 0.83 and 0.95. However under such conditions the fretting loop adopts a quasi-elliptical shape with increasing tangential forces towards the end of each stroke (Fig. 4D–F). The area of the fretting loops over the course of the fretting regime for NiTi are more consistent in comparison to those produced by CoCrMo alloy for all polarisation regimes. The trends in dissipated energy over-time were not consistent with those observed for CoCrMo and were not seen to increase with applied potential.

4. Cumulative Dissipated Energy

Fig. 5A and B shows the cumulative energy dissipation as a function of cycles for CoCrMo and NiTi under different corrosion conditions for CoCrMo and NiTi, respectively. In general, an increase in the total energy dissipated during fretting increased with applied potential and in both material cases was non-linear with the number of cycles. When compared to CoCrMo, the energy dissipated during fretting for NiTi materials was greater.

The relationship between cumulative dissipated energy and total volume loss for CoCrMo and NiTi alloys at all polarisation potentials is shown in Fig. 5C and D, respectively. For CoCrMo an increasing trend in total volume loss and total energy dissipated was observed. This relationship was not observed in NiTi alloy under all polarisation potentials (Fig. 5C and D).

4.1. Wear Scar Morphology

Representative wear scar morphology for both alloys under all polarisation conditions is shown with both OM and VSI images in Fig. 6. Independent of the wear scar size, wear scar morphology is comparable over all polarisation conditions for CoCrMo alloy (Fig. 6A–C). CoCrMo wear scar for all conditions is characteristic of a gross slip regime in agreement with fretting loop appearance (Fig. 4A–C). The wear scar depth, as exhibited in the VSI images, appears to increase with

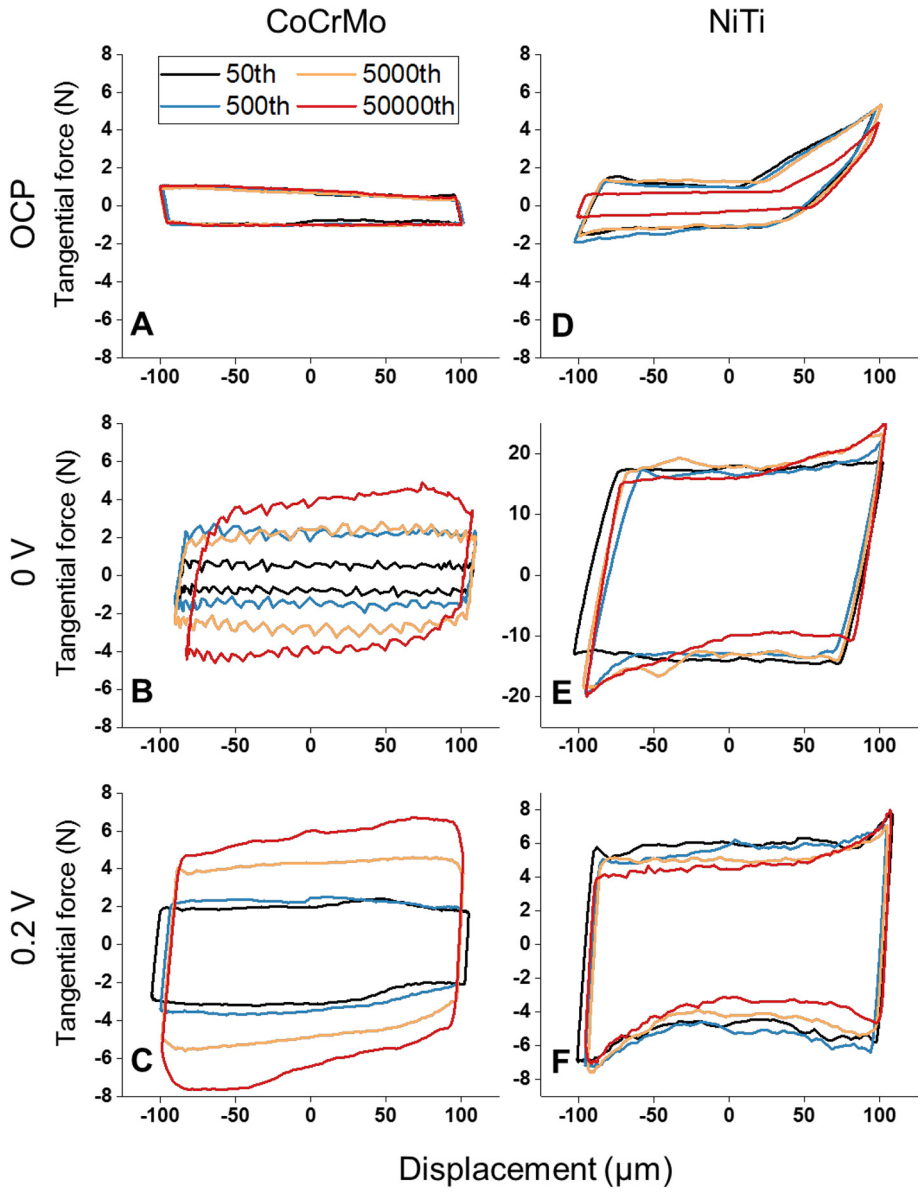

Fig. 4. Representative fretting loops from the 50th and 50,000th cycle for CoCrMo and NiTi alloy in polarisation regimes at OCP and held at 0 V and 0.2 V.

polarisation potential. However for NiTi alloy, wear scar morphology appears to be affected by polarisation potential. At OCP, the wear scar directionality is relatively clear – parallel to the cylinder length for the top sample and perpendicular for the base (Fig. 6D). As polarisation potential is increased, the wear scar surface became more heterogeneous and the directionality became indistinguishable at 0.2 V (Fig. 6E, F). CoCrMo alloy typically exhibited a classically abrasive wear scar morphology whilst NiTi showed an increasingly adhesive scar morphology with increasing potential. In summary, the inherent wear scar morphology was overtly altered in NiTi fretting by polarisation, but not for CoCrMo alloy.

4.2. Corrosion Results

4.2.1. Evolution of OCP

Representative OCP readings for both CoCrMo and NiTi alloy are shown in Fig. 7A. The OCP prior to initiation of sliding was more noble for CoCrMo when compared to NiTi. For both alloys, there is a sharp decrease in OCP upon initiation of sliding indicative of abrasion of the passive layer. There is a persistent decrease in OCP for CoCrMo and NiTi over time. Recovery of the OCP was observed when fretting was ceased although did not recover to values observed before the application of fretting suggesting changes in oxide chemistry and increased susceptibility to corrosion [23,29,43,51].

4.2.2. Potentiostatic Tests

Representative current transients obtained under potentiostatic conditions (those held at 0 V and 0.2 V) are shown in Fig. 7B. There was a consistent increase in current for both CoCrMo and NiTi at both 0 V and 0.2 V upon initiation of sliding, indicating abrasion of the passive layer. For both alloys an increase in polarisation potential from 0 V to 0.2 V typically resulted in a consistently higher current although this increase was much starker in NiTi. Generally NiTi reached higher sustained currents than CoCrMo (Fig. 7B). The cumulative charge for all experiments is given in Fig. 7C. For CoCrMo, increasing the polarisation potential from 0 V to 0.2 V typically did not result in significant increase in cumulative charge. However, both polarised conditions have greater cumulative charge compared to experiments conducted at OCP. NiTi alloy was more sensitive to an increase in polarisation potential, resulting in a significant increase in both cases – particularly stark when

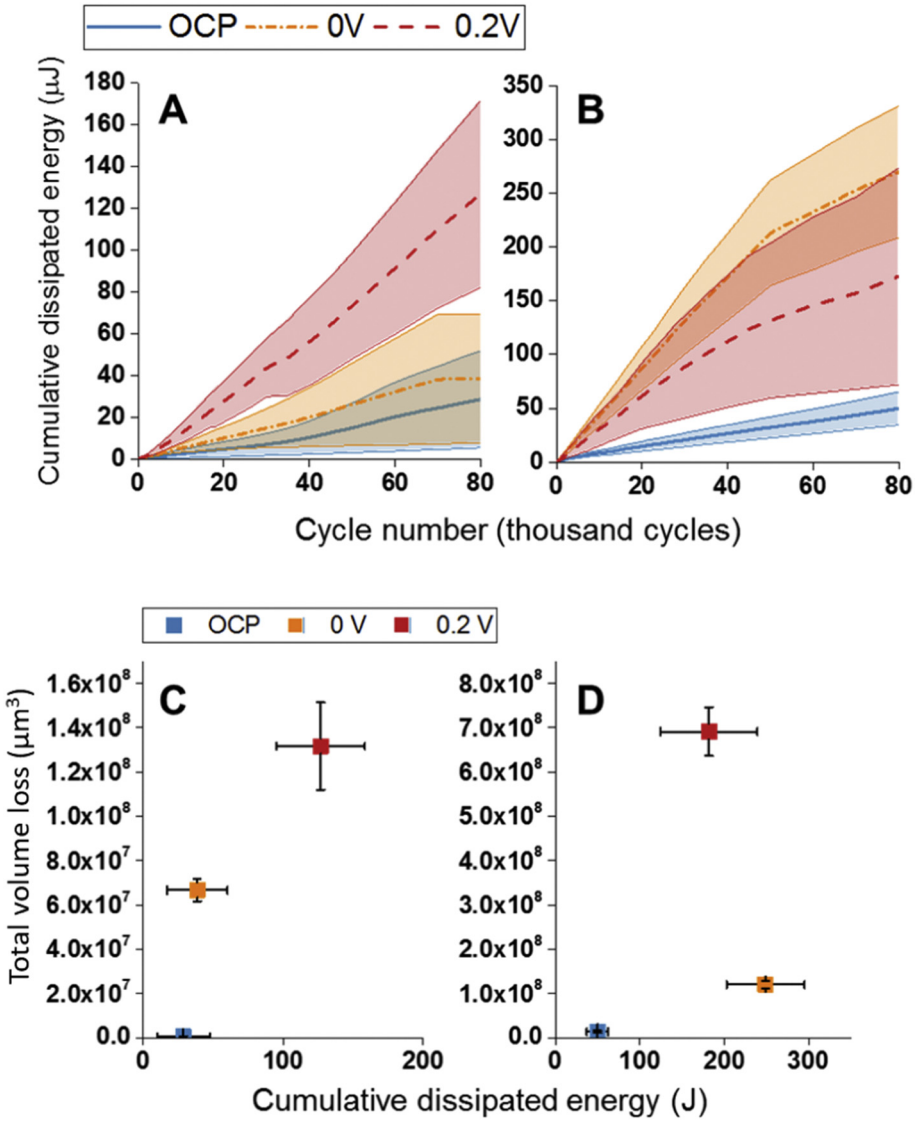

Fig. 5. Cumulative dissipated friction energy over time for (A) CoCrMo and (B) NiTi alloy for fretting-corrosion under OCP and held at 0 V and 0.2 V (n = 3). Cumulative dissipated energy also shown as a function of total wear volume for (C) CoCrMo (red line = linear fit, adj. R^2 = 0.92) and (D) NiTi (red line = exponential fit) alloy. Data shown is mean ± 95% confidence intervals (Panels A and B: shaded area). (For interpretation of the references to colour in this figure legend, the reader is referred to the web version of this article.)

increased to 0.2 V.

4.3. Material Loss

Total material loss (M_{total}) was quantified using VSI and nominal alloy densities. The contributing mechanisms to mass loss are presented later in this paper in Fig. 13. There was no significant difference in total mass loss between the potentiostatic regimes for CoCrMo alloy (0.73 ± 0.42 mg at 0 V; 1.21 ± 0.49 mg at 0.2 V). Samples from both potentiostatic regimes had significantly greater total mass loss vs. those which underwent fretting-corrosion at free corrosion potential (4.70 ± 0.74 μg, $p < .05$ vs. 0 V and $p < .001$ vs. 0.2 V). NiTi alloy appeared to be particularly susceptible to an increase in polarisation potential: total mass loss at 0.2 V (6.68 ± 1.85 mg) was significantly greater than that at 0 V (0.79 ± 0.06 mg, $p < .001$) and OCP (0.09 ± 0.03 mg, $p < .001$). However, total mass loss at OCP and 0 V was not significantly changed. Total mass loss for both CoCrMo alloy and NiTi alloy were relatively similar under both OCP and 0 V regimes. However, at 0.2 V NiTi had a mean 5.5-fold increase in total mass loss compared to CoCrMo alloy.

4.4. Wear Scar Chemistry

Wear scar chemical composition and topography was analysed with SEM-EDX. Representative SEM images of the wear scar and SEM-EDX maps of the wear scar chemistry for each polarisation condition for CoCrMo are shown in Fig. 8 and those for NiTi are shown in Fig. 9. Elements such as phosphorus, potassium, calcium and chlorine were seen in the contact areas after fretting-corrosion. For CoCrMo alloy, increasing the polarisation potential from OCP up to 0.2 V resulted in a stronger correlation of chromium with oxygen (Fig. 8C, F, I). Molybdenum signal remained generalised over the whole wear scar under all polarisation conditions. At 0 V only there was localised formation of phosphorous which was more generalised at both OCP and 0.2 V. Under OCP conditions, a build-up formed at the edge of the wear scar which is noticeably absent under both 0 V and 0.2 V conditions. Interestingly, the element signals present differ between polarisation potential: calcium is only detected at OCP and potassium is solely detected at 0 V.

For NiTi alloy, in all polarisation conditions, the formation of complexes within the fretting contact were dominated by titanium (Fig. 9; Panel C, F and I). Formation of titanium oxide film occurred

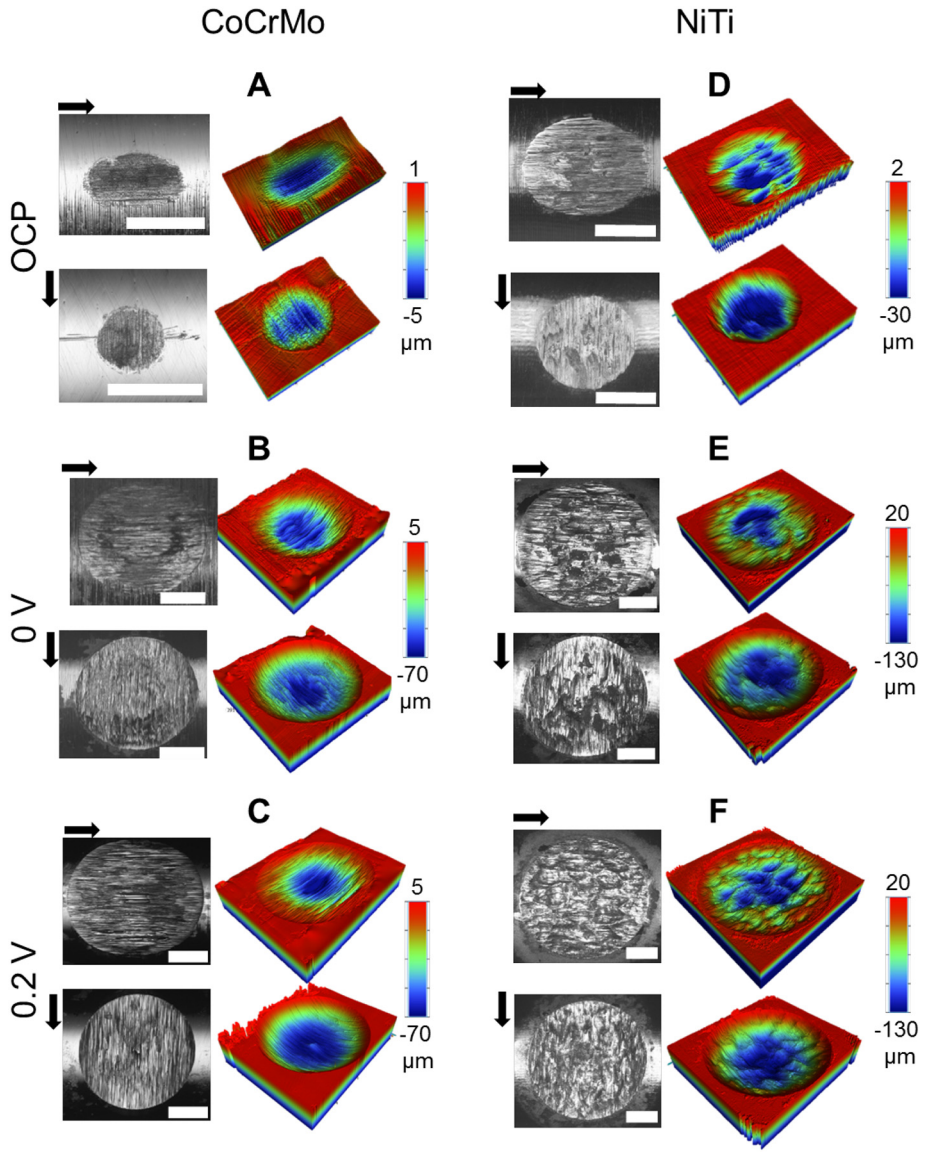

Fig. 6. Wear volume loss and wear scar morphology as shown by VSI and microscopy respectively for CoCrMo and NiTi in all polarisation conditions. (A) CoCrMo at OCP. (B) CoCrMo at 0 V potentiostatic. (C) CoCrMo at 0.2 V potentiostatic. (D) NiTi at OCP. (E) NiTi at 0 V potentiostatic. (F) NiTi at 0.2 V potentiostatic. Scale bar for microscopy images = 500 μm. Top and bottom images for each panel represent top and bottom samples respectively. Sliding direction is horizontal for the top samples and vertical for the bottom samples (arrows).

generally over the wear scar, whereas sulphur and carbon complexes formed in specific locations at OCP and 0.2 V respectively. Increasing the polarisation potential from instigates inherent changes in wear scar chemistry. At OCP, oxygen correlates with sodium, phosphorous, calcium, potassium and chlorine. However at 0 V and 0.2 V, carbon is detected which is not present at OCP. Conversely sodium, sulphur and calcium are only detected at OCP and are not present at 0 V and 0.2 V (Fig. 9C, F, I). Contrary to CoCrMo, for NiTi a build-up of predominantly elements only contained within the serum-free media (O, C, P, K) rather than those contained within the bulk metal (Ni, Ti) can be observed at anodic polarisation conditions around the edge of the contact whereas this was absent at OCP (Fig. 9; Panels A, D and G).

4.5. Ion Release Into Media

Ion release to the electrolyte was determined through ICP-MS for CoCrMo and NiTi alloys at each polarisation condition (OCP, 0 V and 0.2 V) after centrifugation. The composition of ion release is shown in Fig. 10. For CoCrMo, the total levels of ions released to the media was not significantly different across all polarisation regimes (11.1 ± 4.7 ppm, 2.9 ± 1.3 ppm and 10.5 ± 2.8 ppm for OCP, 0 V and 0.2 V respectively). However the composition of the ion release was affected. Ion release for fretting-corrosion of CoCrMo was dominated by cobalt in both potentiostatic polarisation conditions; 80% at 0 V and 92% at 0.2 V. Ion dissolution to media was dominated by chromium for CoCrMo alloy at OCP, at a level of 89% with Co dissolution dropping significantly to 2% ($p < .001$).

Total ion release for NiTi alloy was also not found to be different at OCP (0.22 ± 0.05 ppm) compared to 0 V (1.9 ± 0.4 ppm). However, the total ion release at 0.2 V (160 ± 79.6 ppm) was much higher and was significantly increased compared to both that at OCP and 0 V ($p < .01$). Ion release for NiTi alloy was approximately stoichiometric at OCP (57% Ni), but under electrochemical polarisation was dominated by Ni, increasing with polarisation potential; 71% at 0 V and 99% at 0.2 V. The proportion of Ni ions which were released into the media was significantly increased at both 0 V ($p < .05$) and 0.2 V ($p < .001$) versus OCP.

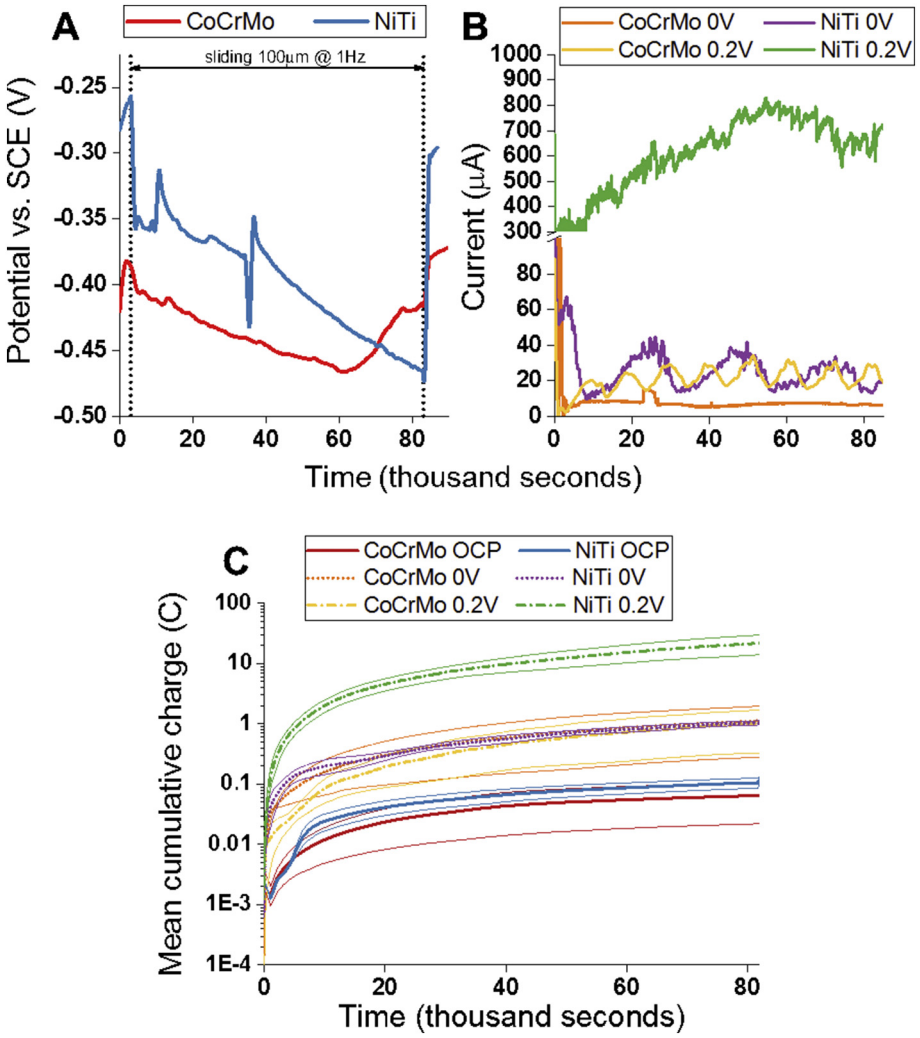

Fig. 7. (A) Representative open circuit potential (OCP) readings for CoCrMo and NiTi cross cylinder fretting corrosion. Samples were left to reach free potential for 1 h prior to initiation of sliding for 80,000 cycles at 1 Hz. Subsequently, samples were left for 1 h to recover. Linear polarisation measurements (OCP ± 0.02 mV) were conducted every 1000 s for the duration of the experiment. (B) Representative current transients for potentiostatic experiments held at 0 V and 0.2 V. (C) Cumulative charge for all experiments using Stern-Geary relationship with intermittent LPRs to give I_{corr} for OCP experiments. Data shown is mean ± SEM (shaded area).

4.6. Particle Morphology and Composition

Particle morphology and composition was determined with SEM-EDX imaging. For CoCrMo alloy, increasing polarisation potential had a clear impact on particle morphology. At OCP, for all three tests which were performed, particles tended to be in the micron to sub-micron range and were typically smooth and relatively heterogeneous (Fig. 11A). However, when analysed with SEM-EDX, it was not possible to identify any of the bulk metal elements (Co, Cr and Mo) in the particles after removal of soluble salts by washing with ultrapure water (Fig. 11B). Instead, particles showed signals for oxygen, phosphorous and calcium which are all elements present in the serum-free culture medium electrolyte.

For the potentiostatic conditions, at 0 V particles were typically in the micron to sub-micron range, although some larger 'clusters' were identified (Fig. 11C). Chromium, oxygen and phosphorous rich particles were observed, with no evidence of cobalt being observed. Silicon was also detected which was not present in the wear scar interface of the bulk alloys (Fig. 11D). At 0.2 V, the particle morphology appeared to be less 'particulate' and was generally seen to have clusters of larger particles which were more irregular in shape (Fig. 11E). The chemistry of the particles was relatively equivalent to that at 0 V, with good correlation of chromium, oxygen and phosphorous and an absence of cobalt (Fig. 11F).

For NiTi alloy, at OCP particles were typically smooth, uniform and in the single micron to nanoparticle range although this was occasionally interspersed with large multi-micron scale particles (Fig. 12A). The smallest particles were comprised of bulk NiTi, demonstrating EDX signals for both nickel and titanium (Fig. 12B). Larger particles showed oxide signals. At 0 V, particle morphology was generally flakier; particles were rougher and flatter than in in OCP condition (Fig. 12C). Particles ranged in nanometres to multi-micron in size. Composition at 0 V polarisation was similar to that at OCP, where particles typically demonstrated nickel, titanium and oxygen signals (Fig. 12D). Fretting tests at 0.2 V polarisation were markedly different from the other conditions in that they tended to be larger and had a heterogeneous more 'powdery' appearance (Fig. 12E). Nickel signals from EDX tended to be weaker than those from particles at other polarisation conditions and also showed complexing with calcium and phosphorus in addition to oxygen (Fig. 12F).

5. Discussion

This study has investigated the role of fretting -corrosion on the degradation of materials commonly used in biomedical applications. The resultant ionic and particulate debris has been quantified as a function of applied over-potential. Fretting-corrosion at the stent-strut interface has been observed clinically, with the roles of metal ion and particle release hypothesised to contribute to ISR processes [16]. Whilst the role of metal ion release into the cardiovascular environment and prevalence in clinical complications is not fully understood, it is accepted that toxic and sub-toxic release of metal derived debris may induces some adverse clinical effects. Furthermore, pre-clinical assessment studies typically treat wear and corrosion in isolation [10,14],

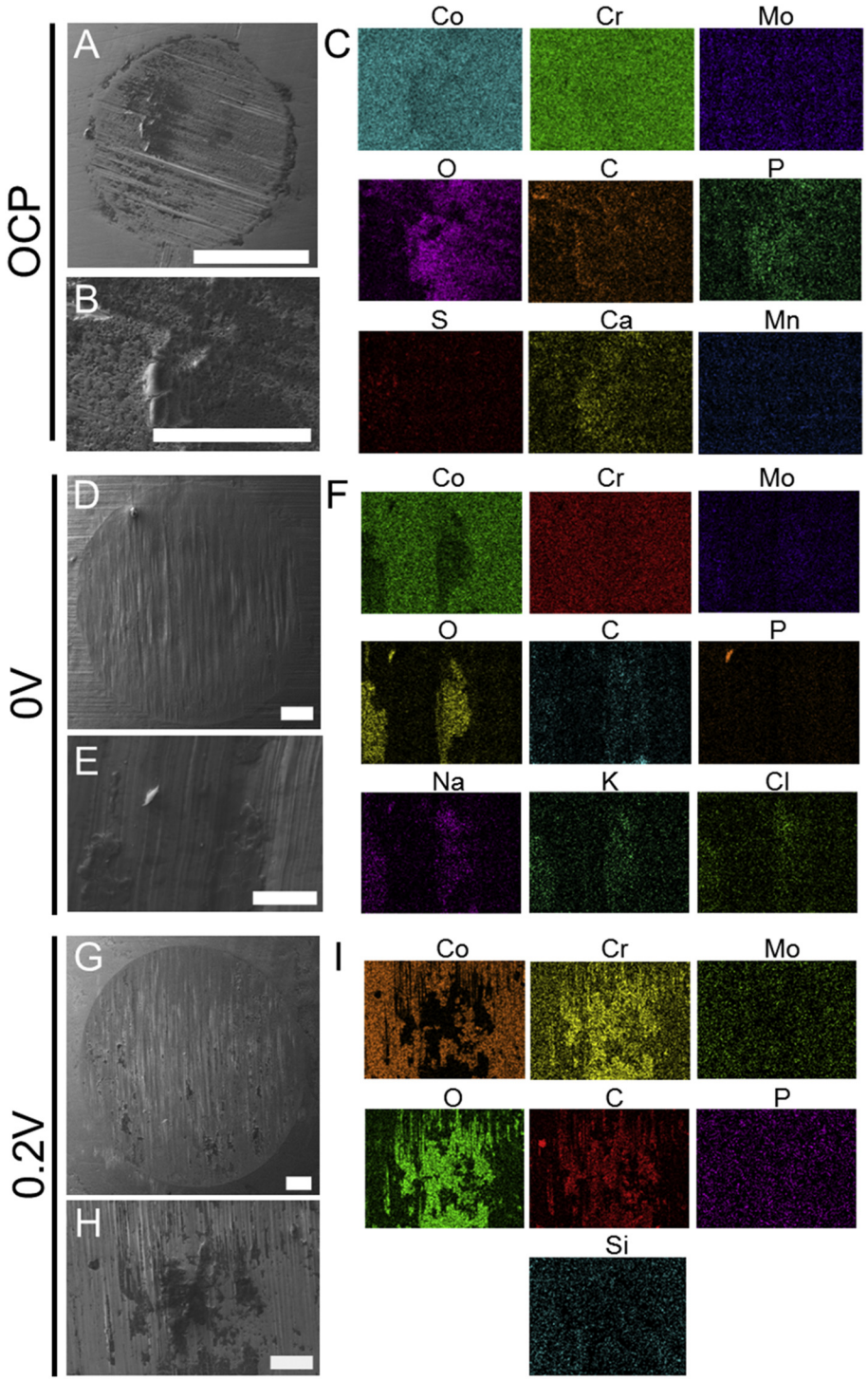

Fig. 8. Representative SEM images and SEM-EDX maps for CoCrMo alloy for all polarisation conditions. (A) SEM image of complete wear scar at OCP. (B) SEM image of wear scar detail at OCP. (C) SEM-EDX map for wear scar chemistry at OCP. (D) SEM complete wear scar 0 V. (E) SEM detail wear scar 0 V. (F) SEM-EDX map 0 V. (G) SEM complete wear scar 0.2 V. (H) SEM detail wear scar 0.2 V. (I) SEM-EDX map 0.2 V. Panels A, D, G: scale bar = 200 μm. Panels B, E, H: scale bar = 100 μm.

only revealing part of the story concerning the degradation of metallic surfaces. Key findings from this study can be summarised as follows:

i) The synergistic interaction of wear and corrosion are inevitable at contacting metal-metal interfaces when subjected to micro-motion in a conductive biological environments. The presence of fretting increasing the rates of corrosion. This leads to the production of metallic ions and particulates; the nature of which are dependent on the tribological and corrosive conditions applied.

ii) The electrochemical parameters used to facilitate measurements of current transients associated with fretting-corrosion can significantly affect the mechanisms of degradation and the nature of the debris generated. This raises question around the suitability of imposing electrochemical potentials in the preclinical assessment of materials and how we interpret such data.

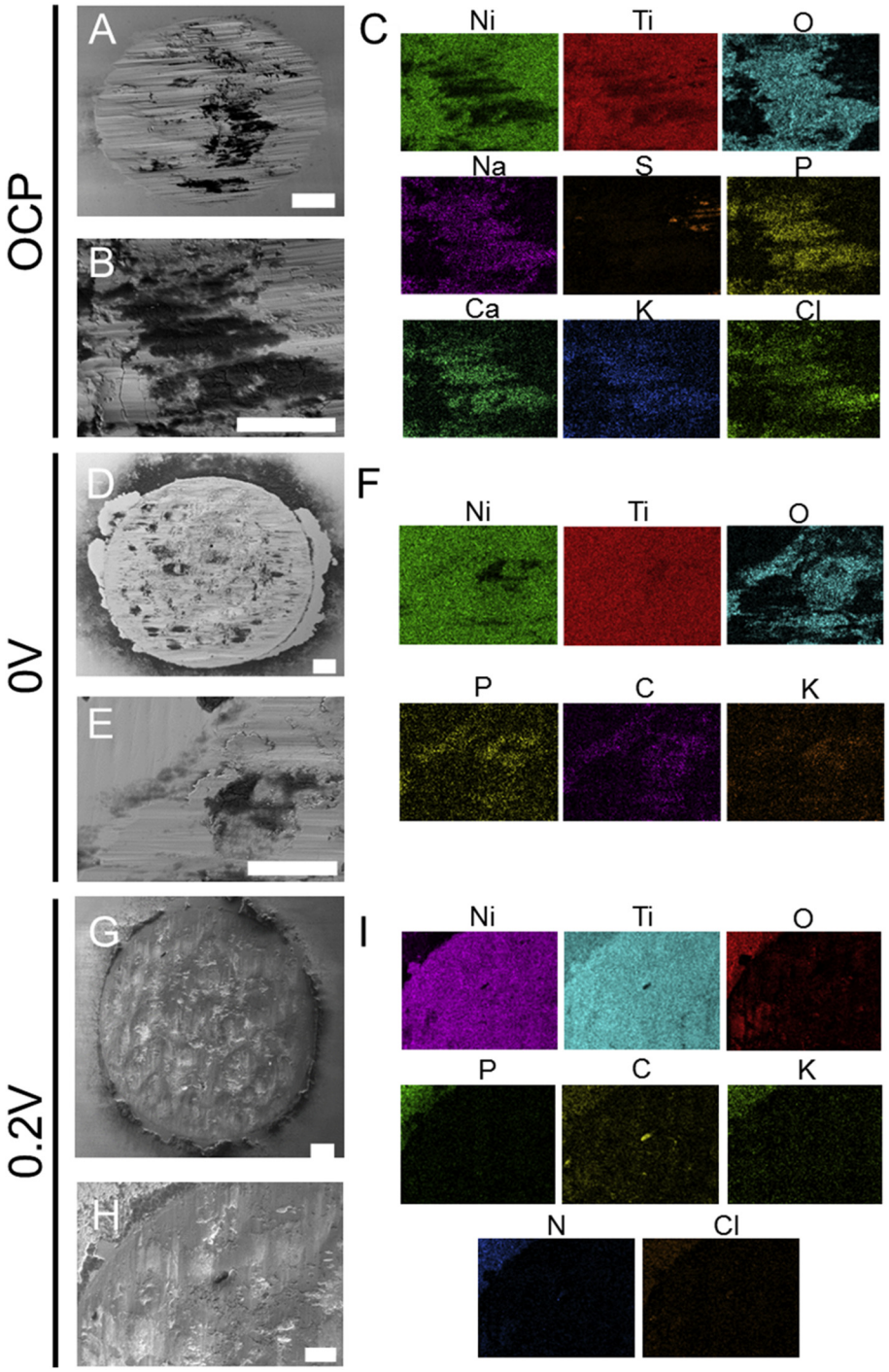

Fig. 9. Representative SEM images and SEM-EDX maps for NiTi alloy for all polarisation conditions. (A) SEM image of complete wear scar at OCP. (B) SEM image of wear scar detail at OCP. (C) SEM-EDX map for wear scar chemistry at OCP. (D) SEM complete wear scar 0 V. (E) SEM detail wear scar 0 V. (F) SEM-EDX map 0 V. (G) SEM complete wear scar 0.2 V. (H) SEM detail wear scar 0.2 V. (I) SEM-EDX map 0.2 V. Panels A, D, G: scale bar = 200 μm. Panels B, E, H: scale bar = 100 μm.

5.1. The Role of Applied Potential on Degradation Mechanisms

The degradation mechanism in fretting-corrosion arises from a synergistic interaction between mechanical wear (M_{mech}) and corrosion due to intermittent depassivation (M_{chem}) [29]. Considering this, the relative contributions to total material loss in fretting-corrosion can be estimated using the Eqs. (3)–(5). M_{mech} is subdivided into M_{wear}, a purely mechanical component, and M_{cw} representing the synergy between corrosion and wear (corrosion-enhanced wear). Equally M_{chem} is subdivided into M_{corr}, a purely chemical component, and M_{wc} representing the synergy between wear and corrosion (wear-enhanced corrosion) [45]. This approach is widely use in the area on tribo-corrosion to estimate material mass loss contributions. Bryant and Neville [45] have recently provided a detailed analysis of the approaches in calculating material loss mechanisms in fretting-corrosion contacts and the limitations of this approach [45,52]. Corrosion currents (Fig. 7) were converted into corrosion mass losses where 'm' is the mass liberated at the anode, 'Q' is the charge passing through the WE, 'M' is the molar mass of the element, 'z' is the dissolution valence and 'F' is Faraday's constant equal to 96,480 C mol^{-1}. For each alloy, it was

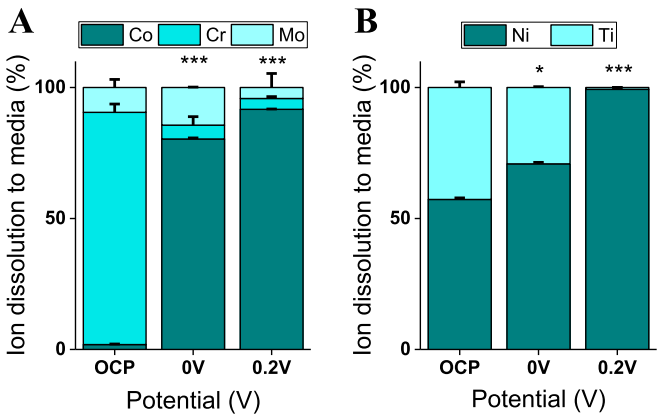

Fig. 10. Proportion of ion release as measured through ICP-MS for (A) CoCrMo alloy and (B) NiTi alloy. *p < .05, ***p < .001, one-way ANOVA with post-hoc Tukey test for (A) Co ions and (B) Ni ions. Data shown is mean ± 95% confidence intervals.

assumed that there was stoichiometric dissolution of the component elements, giving molar mass (M) as 58.0 g·mol^{-1} for CoCrMo and 53.8 g·mol^{-1} for NiTi. Equally, the dissolution valence (z) was assumed to be 2.0 for CoCrMo and 2.9 for NiTi. Applying Faraday's law to the electrochemical data recorded throughout the duration of the fretting-corrosion experiments allowed conversion to mass loss equal to chemical wear (M_{chem}). The total mass loss (M_{total}) was determined using VSI and known alloy density and their difference represented mass loss due to mechanical wear (M_{mech}).

$$M_{total} = M_{mech} + M_{chem} \quad (3)$$

$$M_{mech} = M_{wear} + M_{cw} \quad (4)$$

$$M_{chem} = M_{corr} + M_{wc} \quad (5)$$

$$m = \frac{Q \times M}{z \times F} \quad (6)$$

Fig. 13 shows the total mass loss (M_{total}) and their contributors using the approach described above (Eq. (6)) for CoCrMo and NiTi alloys. At OCP, 0 V and 0.2 V, CoCrMo material loss mechanisms were dominated by corrosion related processes. However with increasing applied polarisation potential the role of mechanical contributors in the fretting-corrosion system increased (Fig. 13A). As mentioned above, M_{mech} still contains a corrosive contributor. Corrosion enhanced wear processes, whereby mechanical material losses are enhanced through corrosion processes (e.g. by increased surface roughness), may contribute to this increase. With increased applied potential, higher currents were observed which will in turn influence the nature of topography within the contact as evidenced in Fig. 6.

Conversely, NiTi operated in a regime where M_{mech} was dominant, with corrosive contributions increases with applied potential due to the increased over-potential driving the magnitude of current evolved during abrasion. An increase in polarisiation potential appears to increase the susceptibility of NiTi to corrosive-dominated wear as demonstrated by the increase in corrosion current coupled with no change in dissipated frictional energy. Nevertheless, the wear degradation pathway tended towards a more wear-dominant regime with increasing polarisation potential as exhibited by the relative contributions to wear (Fig. 13). However, the fretting-corrosion system exists as a synergy of wear and corrosion: although the corrosion currents exponentially increased with polarisation potential, mechanical depassivation is still required for this wear-enhanced corrosion. Lukina et al. demonstrated that under fretting corrosion, NiTi is particularly susceptible to very high corrosion currents compared to other alloys such as biomedical titanium and CoCrMo [53]. Kosec et al. also concluded NiTi was susceptible to increased material degradation under wear-corrosion synergy conditions as opposed to static corrosion due to cyclic depassivation of the oxide film [54]. In the case of overlapping NiTi stents, Trépanier et al. showed that the effect of wear on corrosion was comparable between stainless steel and NiTi [55]. However, in this case, the wear-corrosion synergy was not considered and specimens underwent fretting wear damage and then were subsequently subjected to cyclic polarisation testing. NiTi is comparable to stainless steel in its ability to repassivate wear damage to the stent surface, but the present study shows that NiTi is more susceptible than CoCrMo to the wear-corrosion synergy under polarisation.

5.2. The Roles of Applied Potential on Fretting Mechanisms

The effect of applied over potential on the tribology at an interface has been well documented in sliding contacts. Ponthiaux et al. [56] showed the variation of the coefficient of friction, μ, at different applied potentials and hypothesised the coefficient of friction to be linked to lowest zero current potential because 'mechanical depassivation in the contact area is at maximum and leads to the largest total active area'. They also hypothesised that higher coefficient of friction can be associated with passivity. Within a biotribological context, Yan et al. [51] demonstrated the roles between applied potential and the coefficient of friction, attributing the complex behaviour to tribo-chemical processes occurring at the metal – protein level.

A similar observation has been observed in this study. For CoCrMo alloy subjected to fretting-corrosion, tangential forces and cumulative dissipated energy were seen to increase with increasing applied potential. This is in line with other tribocorrosion studies on CoCrMo where the coefficient of friction correlates with applied over-potential [51,57]. In our case we have considered dissipated energy, which considers frictional forces and displacement at the interface, due to the difficulties in determining friction within a fretting contact [58–60]. Interestingly, when CoCrMo was subjected to polarisation at 0 and 0.2 V, the tangential forces increased with increasing number of cycles (Fig. 4B and C). It is conceivable that frictional forces increase with increasing number of cycles due to the development of the contact area over the 80,000 cycles. The final nominal contact area is considerably larger than the initial Hertzian contact area calculated with an increased confirmation of the surfaces.

It is evident that the development of the contact area is linked to the corrosion conditions at the contact and will be enhanced by the accelerated corrosion at the interface. In the literature, coefficients of friction ranging from μ = 0.1 to 1 have been quoted for CoCrMo in sliding interfaces [57]. Furthermore the formation of and retention of oxides within the contact will influence the evolving tribology; although their roles in a fretting-corrosion contact past third body effects are not well understood and significantly different in nature to tribo-chemical reactions in sliding contacts.

In the case of NiTi alloy, the effect of applied potential from 0 V and 0.2 V was not as apparent as for CoCrMo alloy. All NiTi fretting loops showed a gross-slip regime, with some interesting observations between those at OCP and at an applied potential. A slight decrease in $\frac{\delta_s}{\delta_d}$ was observed when compared to CoCrMo-CoCrMo interfaces likely due to the decreased reduced modulus of the NiTi-NiTi contact. As a result, a component of elastic deformation was introduced at the interface, although remained well within the gross-slip criteria as outlined by Fouvry [44]. For all three instances of the experiment conducted at OCP the fretting loop shape exhibited a 'tail-like' region on the forward stroke. The reasons for this are not fully understood, but are there are some links between the mechanical and electrochemical processes evident. At the wear scar interface there was very localised formation of sulphurous complexes solely at OCP, perhaps going some way towards explaining the unusual fretting-loop shape – as they are so localised, the tangential force peaks over the course of the fretting cycle as it interacts with them. Fretting loops at 0 and 0.2 V presented a more conventional

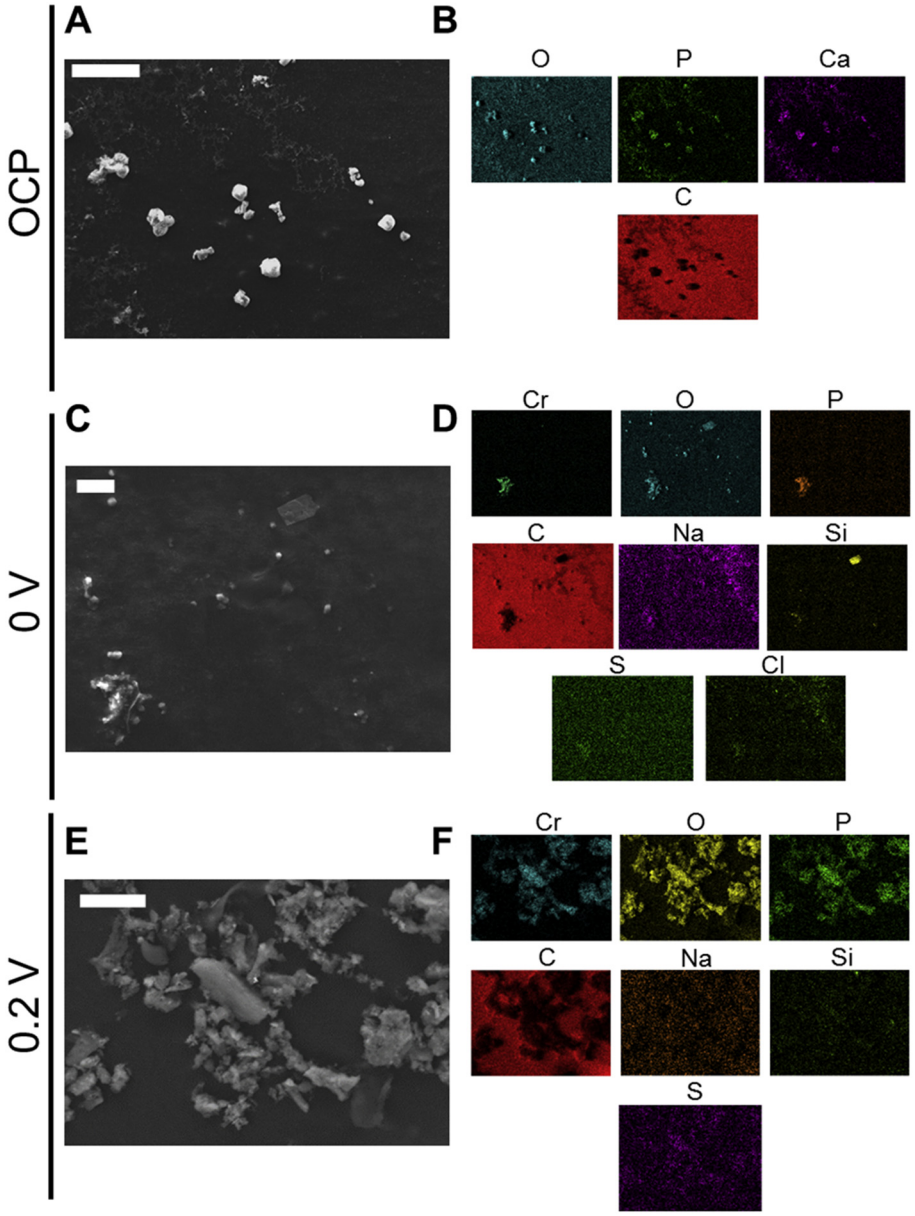

Fig. 11. Representative SEM images and SEM-EDX maps for wear particles from CoCrMo alloy fretting experiments. (A) SEM image of wear particles from CoCrMo fretting at OCP. (B) SEM-EDX map for particle chemical composition at OCP. (C) SEM wear particles CoCrMo 0 V. (D) SEM- EDX map wear particles CoCrMo 0 V. (E) SEM wear particles CoCrMo 0.2 V. (F) SEM-EDX map wear particles CoCrMo 0.2 V. Scale bar for all images = 25 μm.

appearance with evidence of plastic pile up at the edges of the contact, causing the tangential force to increase rapidly towards the end of the stroke [59]. This is supported by Fig. 9 which shows evidence of debris build-up at the edges of the contact. Due to the lack of fretting loop analysis for NiTi in physiological media, this phenomenon cannot be entirely explained. The root cause for this is unclear and further work to understand if this relates to a strain related transformation of the NiTi or localised build-up of debris within the contact is needed. No trend in the magnitude of tangential forces at the different polarisation conditions and with increasing number of cycles could be observed, in contrast to CoCrMo. Overtime, the rate of cumulative energy dissipation was seen to decrease suggesting a change in the degradation rate or mechanism at the interface. This may arise from the unique austenitic – martensitic strain-rate dependant transformation characteristics that NiTi alloys possess [61]. It is conceivable that cyclic loading and fatigue at the interface will induce cumulative changes in the subsurface microstructure effecting the evolution of mechanical and corrosive damage over time.

5.3. The Role of Applied Potential on Ionic and Particulate Debris Formation

In both metallic alloy cases, the debris and ion release was altered in terms of both chemistry and morphology with the application of electrochemical over-potential. The elements making up the bulk metal substrate (Co, Cr and Mo) were not detected when undertaking SEM-EDX analysis at OCP, but instead provided signals for O, P and Ca. These were also present on the wear scar surface, indicating that at OCP the removed wear debris consists of the passive layer formed continuously from abrasion and retained in the contact during fretting [62]. With the application of over-potential, the elemental composition of the debris was seen to vary when compared to debris retrieved OCP. Cr, O and P rich debris was observed, similar to that retained within the contact. A similar observation was seen of the NiTi, with the application

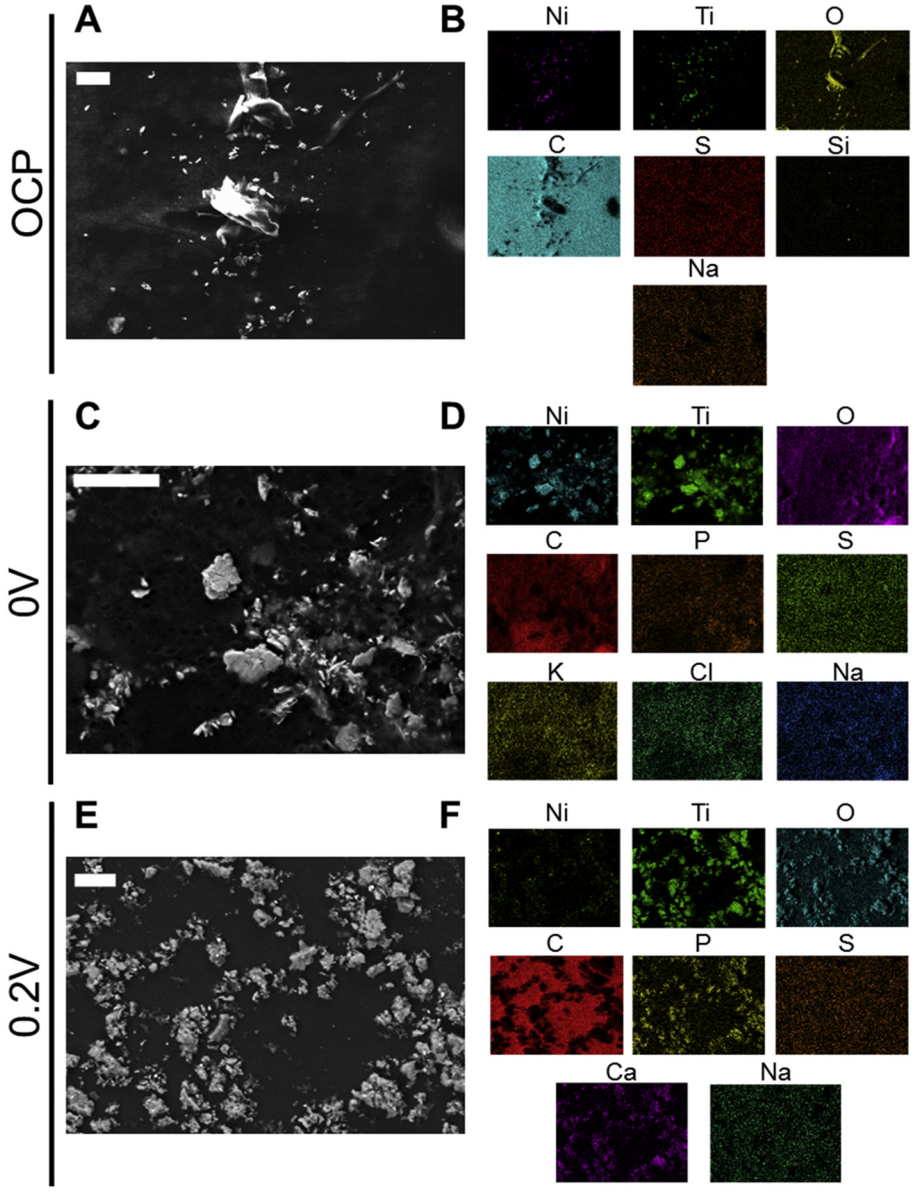

Fig. 12. Representative SEM images and SEM-EDX maps for wear particles from NiTi alloy fretting experiments. (A) SEM image of wear particles from NiTi fretting at OCP. (B) SEM-EDX map for particle chemical composition at OCP. (C) SEM wear particles NiTi 0 V. (D) SEM-EDX map wear particles NiTi 0 V. (E) SEM wear particles NiTi 0.2 V. (F) SEM-EDX map wear particles NiTi 0.2 V. Scale bar for all images = 25 μm.

of over-potential influencing the nature and chemistry of the debris produced. At OCP, debris mainly consisting of Ni, Ti, and O was observed. The nature of the debris produced was seen to be altered with the application over potential during fretting-corrosion, with Ti, O, P and Ca rich particulates being observed at 0.2 V. Without a doubt, the application of an applied electrochemical potential influences the nature of the debris generated at an interface, intrinsically linked to the changes tribological processes discussed above and the changes in passive film chemistry. It is well established that the application of over-potential influences the nature and quantity of preferentially absorbed species on a surface, the thickness of the oxide film and thermodynamic driving forces for specie migration across the oxide layer. All of these factors will synergistically interact with the tribological processes, influencing the evolving degradation mechanism and nature of the debris produced. Whilst there is not a great deal of literature observing the nature and chemistry of debris derived from fretting-corrosion interfaces, the observations for CoCrMo correlate well with particle analysis retrieved from in-vivo orthopaedic implants. Cr and P rich particles have been observed in peri-implant soft tissues and hypothesised to arise from fretting interfaces which is consistent with this study [63]. The nature NiTi debris is still yet to be fully understood.

Perhaps one of the most interesting observations made in this study is the variation in ion release stoichiometry with applied over-potential. For CoCrMo-CoCrMo fretting interfaces, the ion release stoichiometry changed from chromium-dominated to cobalt-dominated with the proportion of cobalt ions increasing with polarisation potential. Similarly for NiTi-NiTi interfaces, this went from a near stoichiometric release of Ni and Ti to a Ni dominated solution. This may be explained by the reliance of biomedical alloys to form a passive surface layer to protect against corrosion, the changes in the oxide film characteristics and nature of species absorbed at the interface as a result of polarisation [26]. In the particular case of CoCrMo and NiTi, this is typically a chromium-oxide and titanium-oxide rich layer respectively [64,65]. Cyclic abrasion of the surfaces and retention of the debris within the interface is supported by both the wear scar chemistry and that of the wear particles. In both cases a correlation between the elemental

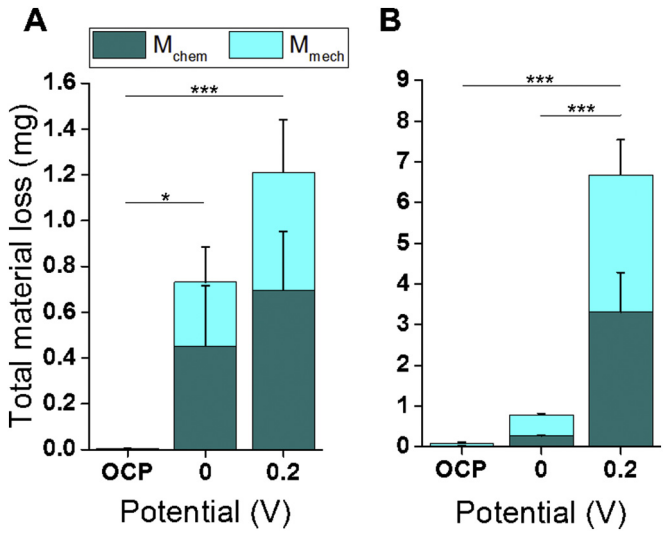

Fig. 13. Relative contributions to total wear in terms of mechanical and chemical degradation mechanisms for (A) CoCrMo and (B) NiTi alloy in three polarisation regimes (OCP, 0 V and 0.2 V) during 80,000 fretting cycles ($n = 3$). Data shown is mean ± 95% confidence intervals. Total wear significance shown with one-way ANOVA with post-hoc Tukey test, $*p < .05$, $***p < .001$.

composition of the debris and stoichiometry could be observed suggesting. For CoCrMo-CoCrMo contacts, where Cr rich debris was observed (Fig. 11C and E), Cobalt dominated ion release was observed. This suggest that the mobility and of Co and Cr at the interfaces differs based on the electrochemical and tribological conditions at the interface. A similar observation was made for NiTi-NiTi interfaces. Ni dominated ion release was observed at 0.2 V whereas the debris was Ti, O, P and Ca rich. In both cases, Cr and Ti are thermo-dynamically favourable reactions contributing the reformation of oxide layer once abraded [66]. An initial release of Ni and Co will likely occur when the nascent metallic surface is exposed to the electrolyte until an effective oxide layer is formed, enabling the soluble Ni and Co to migrate from the interface. This will depend on the electrode potential and pH at the interface. This further points to the importance of considering the nature of the test environment and experimental conditions on the debris generation mechanisms at an interface.

The enhanced metal ion release due to tribological processes has been reported mainly for sliding contacts, which significantly differ to fretting-corrosion interfaces. Espallargas et al. showed that ion release was dominated by cobalt under sliding-corrosion at OCP and cathodic and anodic polarisation [35]. However, the interface in this study was a sliding (6 mm stroke length) CoCrMo-alumina interface as opposed to a fretting CoCrMo-CoCrMo contact. In a hip implant head/cup large sliding interface ion dissolution was shown to be stoichiometric rather than cobalt-dominated [67]. Molybdenum in terms of ion release, wear scar chemistry and presence in wear particles also appeared to be relatively unaffected by polarisation. However it has previously been shown that molybdenum dissolution is significantly impacted by presence of proteins which were absent from this study [35,49].

5.4. Concluding Remarks

Metallic biomaterials are commonly and widely used for cardiovascular stents and well as other areas of biomedical engineering. Although there is in vivo evidence of wear debris release at the strut interface of braided designs [12,68], to the authors' knowledge there is no literature detailing the links between fretting-corrosion processes and the nature of the resultant debris. To investigate tribocorrosion mechanisms in biomaterials, studies have used potentiostatic polarisation to exacerbate material degradation during fretting. This study shows that the nature of the wear debris, from particle chemistry and morphology to ion release, is affected by the polarisation potential. In the case of CoCrMo, the wear debris was intrinsically altered during polarisation under fretting despite the maintenance of the tribological and electrochemical characteristics. However NiTi was particularly susceptible to wear-enhanced corrosion as polarisation potential was increased, affecting the tribocorrosion mechanism itself and the wear debris.

Gaining an appreciation of the stent in the physiological environment is imperative to elucidating the material degradation mechanisms occurring in stents in vivo and the biological impact of released debris. As proven in hip orthopaedic implants, wear debris and its morphology and composition may have unexpected and devastating consequences for patients [14,17,69]. In the case of vascular stents, it has been shown that fretting-corrosion and local release of wear debris to tissues occurs in vivo [12,68]. This is hypothesised to be a compounding factor in the most common mechanism of stent failure, in-stent restenosis which is a biologically mediated phenomenon. Studies aiming to understand the biological effects of fretting-corrosion must therefore attempt to replicate the physiological scenario. This study shows that undertaking fretting-corrosion experiments under potentiostatic control as opposed to at the materials open circuit potential both CoCrMo and NiTi alloys affected the degradation mechanisms and released wear debris. It can be appreciated that useful triboelectrochemical techniques may inherently alter the system. Future work in this area will be focussed on the biological impact of wear debris under different polarisation regimes and the compounding factors of presence of serum proteins and inflammatory mediators.

Conflicts of Interest

The authors have no conflicts of interest to disclose.

Funding Sources

This work was supported by the Engineering and Physical Sciences Research Council (EP/P009662/1).

References

[1] D. Buccheri, D. Piraino, G. Andolina, B. Cortese, Understanding and managing in-stent restenosis: a review of clinical data, from pathogenesis to treatment, J. Thorac. Dis. 8 (10) (2016) E1150–E1162.
[2] J. Naghi, E.A. Yalvac, A. Pourdjabbar, L. Ang, J. Bahadorani, R.R. Reeves, E. Mahmud, M. Patel, New developments in the clinical use of drug-coated balloon catheters in peripheral arterial disease, Med. Devices (Auckl) 9 (2016) 161–174.
[3] H.C. Lowe, S.N. Oesterle, L.M. Khachigian, Coronary in-stent restenosis: current status and future strategies, J. Am. Coll. Cardiol. 39 (2) (2002) 183–193.
[4] A.K. Mitra, D.K. Agrawal, In stent restenosis: bane of the stent era, J. Clin. Pathol. 59 (3) (2006) 232–239.
[5] G.D. Dangas, B.E. Claessen, A. Caixeta, E.A. Sanidas, G.S. Mintz, R. Mehran, In-stent restenosis in the drug-eluting stent era, J. Am. Coll. Cardiol. 56 (23) (2010) 1897–1907.
[6] J. Xu, J. Yang, S. Sohrabi, Y. Zhou, Y. Liu, Finite element analysis of the implantation process of overlapping stents, J. Med. Devices 11 (2) (2017) pp.021010-021010-9.
[7] K.K. Kapnisis, D.O. Halwani, B.C. Brott, P.G. Anderson, J.E. Lemons, A.S. Anayiotos, Stent overlapping and geometric curvature influence the structural integrity and surface characteristics of coronary nitinol stents, J. Mech. Behav. Biomed. Mater. 20 (2013) 227–236.
[8] Z.M. Jin, J. Zheng, W. Li, Z.R. Zhou, Tribology of medical devices, Biosurf. Biotribol. 2 (4) (2016) 173–192.
[9] D.O. Halwani, P.G. Anderson, B.C. Brott, A.S. Anayiotos, J.E. Lemons, The role of vascular calcification in inducing fatigue and fracture of coronary stents, J. Biomed. Mater. Res. B Appl. Biomater. 100B (1) (2012) 292–304.
[10] C. Trépanier, X.Y. Gong, T. Ditter, A. Pelton, Y. Neely, R. Grishaber, Effect of wear and crevice on the corrosion resistance of overlapped stents, SMST-2006 – Proceedings of the International Conference on Shape Memory and Superelastic Technologies, 2008, pp. 265–276.
[11] Konstantinos Kapnisis, Georgios Constantinides, Harry Georgiou, Daniel Cristea, Camelia Gabor, Daniel Munteanu, Brigitta Brott, Peter Anderson, Jack Lemons, Andreas Anayiotos, Multi-scale mechanical investigation of stainless steel and cobalt–chromium stents, J. Mech. Behav. Biomed. Mater. 40 (2014) 240–251, https://

doi.org/10.1016/j.jmbbm.2014.09.010 (ISSN 1751-6161).
[12] D.O. Halwani, P.G. Anderson, B.C. Brott, A.S. Anayiotos, J.E. Lemons, Clinical device-related article surface characterization of explanted endovascular stents: evidence of in vivo corrosion, J. Biomed. Mater. Res. B Appl. Biomater. 95B (1) (2010) 225–238.
[13] G. Riepe, C. Heintz, E. Kaiser, N. Chakfé, M. Morlock, M. Delling, H. Imig, What can we learn from explanted endovascular devices? Eur. J. Vasc. Endovasc. Surg. 24 (2) (2002) 117–122.
[14] N.J. Hallab, J.J. Jacobs, Biologic effects of implant debris, Bull. NYU Hosp. Joint Dis. 67 (2) (2009) 182.
[15] D. Bingmann, M. Vorpahl, M. Wiemann, H. Brauer, Effects of metal ions on proliferation of aortic smooth muscle cells and myoblastic cells in vitro, Mater. Werkst. 32 (12) (2001) 970–975.
[16] C.C. Shih, S.J. Lin, Y.L. Chen, Y.Y. Su, S.T. Lai, G.J. Wu, C.F. Kwok, K.H. Chung, The cytotoxicity of corrosion products of nitinol stent wire on cultured smooth muscle cells, J. Biomed. Mater. Res. 52 (2) (2000) 395–403.
[17] I. Papageorgiou, C. Brown, R. Schins, S. Singh, R. Newson, S. Davis, J. Fisher, E. Ingham, C.P. Case, The effect of nano- and micron-sized particles of cobalt-chromium alloy on human fibroblasts in vitro, Biomaterials 28 (19) (2007) 2946–2958.
[18] S. Drynda, A. Drynda, B. Feuerstein, J. Kekow, C.H. Lohmann, J. Bertrand, The effects of cobalt and chromium ions on transforming growth factor-beta patterns and mineralization in human osteoblast-like MG63 and SaOs-2 cells, J. Biomed. Mater. Res. A 106 (8) (2018) 2105–2115.
[19] J.T. Ninomiya, S.A. Kuzma, T.J. Schnettler, J.G. Krolikowski, J.A. Struve, D. Weihrauch, Metal ions activate vascular endothelial cells and increase lymphocyte chemotaxis and binding, J. Orthop. Res. 31 (9) (2013) 1484–1491.
[20] C.C. Shih, C.M. Shih, Y.L. Chen, Y.Y. Su, J.S. Shih, C.F. Kwok, S.J. Lin, Growth inhibition of cultured smooth muscle cells by corrosion products of 316 L stainless steel wire, J. Biomed. Mater. Res. 57 (2) (2001) 200–207.
[21] E. Mclucas, Y. Rochev, W.M. Carroll, T.J. Smith, Analysis of the effects of surface treatments on nickel release from nitinol wires and their impact on candidate gene expression in endothelial cells, J. Mater. Sci. Mater. Med. 19 (3) (2008) 975–980.
[22] B. Winn, J.C.D. Quarles, R.K. Marcus, M. Laberge, Nickel ions inhibit α-actin expression and decrease aspect ratio of rat vascular smooth muscle cellsin vitro, Metallomics 3 (9) (2011) 934–940.
[23] D. Royhman, M. Patel, M.J. Runa, M.A. Wimmer, J.J. Jacobs, N.J. Hallab, M.T. Mathew, Fretting-corrosion behavior in hip implant modular junctions: the influence of friction energy and pH variation, J. Mech. Behav. Biomed. Mater. 62 (2016) 570–587.
[24] J.R. Goldberg, J.L. Gilbert, The electrochemical and mechanical behavior of passivated and TiN/AlN-coated CoCrMo and Ti6Al4V alloys, Biomaterials 25 (5) (2004) 851–864.
[25] V. Swaminathan, J.L. Gilbert, Fretting corrosion of CoCrMo and Ti6Al4V interfaces, Biomaterials 33 (22) (2012) 5487–5503.
[26] C. Valero Vidal, A. Igual Muñoz, Electrochemical characterisation of biomedical alloys for surgical implants in simulated body fluids, Corros. Sci. 50 (7) (2008) 1954–1961.
[27] S. Cao, A.I. Muñoz, S. Mischler, Rationalizing the in vivo degradation of metal-on-metal artificial hip joints using tribocorrosion concepts, Corrosion 73 (12) (2017) 1510–1519.
[28] S. Barril, S. Mischler, D. Landolt, Electrochemical effects on the fretting corrosion behaviour of Ti6Al4V in 0.9% sodium chloride solution, Wear 259 (1) (2005) 282–291.
[29] S. Mischler, Triboelectrochemical techniques and interpretation methods in tribocorrosion: a comparative evaluation, Tribol. Int. 41 (7) (2008) 573–583.
[30] V. Swaminathan, J.L. Gilbert, Potential and frequency effects on fretting corrosion of Ti6Al4V and CoCrMo surfaces, J. Biomed. Mater. Res. A 101A (9) (2013) 2602–2612.
[31] M.K. Dimah, F.D. Albeza, V.A. Borras, A.I. Munoz, Study of the biotribocorrosion behaviour of titanium biomedical alloys in simulated body fluids by electrochemical techniques, Wear 294 (2012) 409–418.
[32] S. Hiromoto, S. Mischler, The influence of proteins on the fretting–corrosion behaviour of a Ti6Al4V alloy, Wear 261 (9) (2006) 1002–1011.
[33] Alonso, R. Gil, A. Igual Muñoz, Influence of the sliding velocity and the applied potential on the corrosion and wear behavior of HC CoCrMo biomedical alloy in simulated body fluids, J. Mech. Behav. Biomed. Mater. 4 (8) (2011) 2090–2102.
[34] S. Mischler, P. Ponthiaux, A round robin on combined electrochemical and friction tests on alumina/stainless steel contacts in sulphuric acid, Wear 248 (1) (2001) 211–225.
[35] N. Espallargas, C. Torres, A.I. Muñoz, A metal ion release study of CoCrMo exposed to corrosion and tribocorrosion conditions in simulated body fluids, Wear 332-333 (2015) 669–678.
[36] M. Azzi, J.A. Szpunar, Tribo-electrochemical technique for studying tribocorrosion behavior of biomaterials, Biomol. Eng. 24 (5) (2007) 443–446.
[37] J. Hesketh, X. Hu, Y. Yan, D. Dowson, A. Neville, Biotribocorrosion: some electrochemical observations from an instrumented hip joint simulator, Tribol. Int. 59 (2013) 332–338.
[38] F. Billi, P. Benya, E. Ebramzadeh, P. Campbell, F. Chan, H.A. Mckellop, Metal wear particles: what we know, what we do not know, and why, SAS J. 3 (4) (2009) 133–142.
[39] N. Chakfé, F. Heim, Commentary on 'electrical potentials between stent-grafts made from different metals induce negligible corrosion, Eur. J. Vasc. Endovasc. Surg. 46 (4) (2013) 438–439.
[40] M. Bryant, M. Ward, R. Farrar, R. Freeman, K. Brummitt, J. Nolan, A. Neville, Failure analysis of cemented metal-on-metal total hip replacements from a single centre cohort, Wear 301 (2013) 226–233.
[41] K. Riches, T. Angelini, G. Mudhar, J. Kaye, E. Clark, M. Bailey, S. Sohrabi, S. Korossis, P. Walker, D.J. Scott, K. Porter, Exploring smooth muscle phenotype and function in a bioreactor model of abdominal aortic aneurysm, J. Transl. Med. 11 (1) (2013) 208.
[42] K. Riches, E. Clark, R.J. Helliwell, T.G. Angelini, K.E. Hemmings, M.A. Bailey, K.I. Bridge, D.J.A. Scott, K.E. Porter, Progressive development of aberrant smooth muscle cell phenotype in abdominal aortic aneurysm disease, J. Vasc. Res. 55 (1) (2018) 35–46.
[43] A. Oladokun, M. Pettersson, M. Bryant, H. Engqvist, C. Persson, R. Hall, A. Neville, Fretting of CoCrMo and Ti6Al4V alloys in modular prostheses, Tribol.-Mater. Surf. Interf. 9 (4) (2015) 165–173.
[44] S. Fouvry, P. Kapsa, H. Zahouani, L. Vincent, Wear analysis in fretting of hard coatings through a dissipated energy concept, Wear 203–204 (1997) 393–403.
[45] M. Bryant, A. Neville, Fretting corrosion of CoCr alloy: effect of load and displacement on the degradation mechanisms, Proc. Inst. Mech. Eng. H J. Eng. Med. 231 (2) (2016) 114–126.
[46] A. Neville, J. Hesketh, A.R. Beadling, M.G. Bryant, D. Dowson, Incorporating corrosion measurement in hip wear simulators: an added complication or a necessity? Proc. Inst. Mech. Eng. H J. Eng. Med. 230 (5) (2016) 406–420.
[47] D.C. Silverman, Tutorial on cyclic potentiodynamic polarization technique, Corrosion, NACE International, 98, 1998/1/1/, San Diego, California, 1998, p. 21.
[48] M. Stern, A.L. Geary, Electrochemical polarization: I. A theoretical analysis of the shape of polarization curves, J. Electrochem. Soc. 104 (1) (1957) 56–63.
[49] T.A. Simoes, M.G. Bryant, A.P. Brown, S.J. Milne, M. Ryan, A. Neville, R. Brydson, Evidence for the dissolution of molybdenum during tribocorrosion of CoCrMo hip implants in the presence of serum protein, Acta Biomater. 45 (2016) 410–418.
[50] S. Fouvry, P. Kapsa, L. Vincent, Description of fretting damage by contact mechanics, ZAMM 80 (S1) (2000) 41–44 Journal of Applied Mathematics and Mechanics / Zeitschrift für Angewandte Mathematik und Mechanik.
[51] Y. Yan, A. Neville, D. Dowson, Tribo-corrosion properties of cobalt-based medical implant alloys in simulated biological environments, Wear 263 (7) (2007) 1105–1111.
[52] S.W. Watson, F.J. Friedersdorf, B.W. Madsen, S.D. Cramer, Methods of measuring wear-corrosion synergism, Wear 181-183 (1995) 476–484.
[53] E. Lukina, M. Kollerov, J. Meswania, A. Khon, P. Panin, G.W. Blunn, Fretting corrosion behavior of nitinol spinal rods in conjunction with titanium pedicle screws, Mater. Sci. Eng. C 72 (2017) 601–610.
[54] T. Kosec, P. Močnik, A. Legat, The tribocorrosion behaviour of NiTi alloy, Appl. Surf. Sci. 288 (2014) 727–735.
[55] T. C, G. Xy, D. T, P. A, N. Y, G. R, Effect of wear and crevice on the corrosion resistance of overlapped stents. SMST-2006, International Conference on Shape Memory and Superelastic Technologies, SMST Society, Menlo Park, CA, 2008, pp. 265–275.
[56] P. Ponthiaux, F. Wenger, D. Drees, J.P. Celis, Electrochemical techniques for studying tribocorrosion processes, Wear 256 (5) (2004) 459–468.
[57] A. Igual Muñoz, S. Mischler, Effect of the environment on wear ranking and corrosion of biomedical CoCrMo alloys, J. Mater. Sci. Mater. Med. 22 (3) (2011) 437–450.
[58] K. Kim, J. Geringer, Analysis of energy dissipation in fretting corrosion experiments with materials used as hip prosthesis, Wear 296 (1) (2012) 497–503.
[59] S.R. Pearson, P.H. Shipway, J.O. Abere, R.A.A. Hewitt, The effect of temperature on wear and friction of a high strength steel in fretting, Wear 303 (1) (2013) 622–631.
[60] A.R. Warmuth, P.H. Shipway, W. Sun, Fretting wear mapping: the influence of contact geometry and frequency on debris formation and ejection for a steel-on-steel pair, Proc. Roy. S. A: Math. Phys. Eng. Sci. 471 (2178) (2015).
[61] S. Nemat-Nasser, J.Y. Choi, W.-G. Guo, J.B. Isaacs, M.J.J.O.E.M. Taya and Technology. High Strain-Rate, Small Strain Response of a NiTi Shape-Memory Alloy, 127 (1) (2005) 83–89.
[62] I.M. Feng, B.G. Rightmire, An experimental study of fretting, Proc. Inst. Mech. Eng. 170 (1) (1956) 1055–1064.
[63] A. Di Laura, P.D. Quinn, V.C. Panagiotopoulou, H.S. Hothi, J. Henckel, J.J. Powell, F. Berisha, F. Amary, J.F.W. Mosselmans, J.A. Skinner, A.J. Hart, The chemical form of metal species released from corroded taper junctions of hip implants: synchrotron analysis of patient tissue, Sci. Rep. 7 (1) (2017) 10952.
[64] A.I. Muñoz, S. Mischler, Interactive effects of albumin and phosphate ions on the corrosion of CoCrMo implant alloy, J. Electrochem. Soc. 154 (10) (2007) C562–C570.
[65] I. Milošev, H.H. Strehblow, The composition of the surface passive film formed on CoCrMo alloy in simulated physiological solution, Electrochim. Acta 48 (19) (2003) 2767–2774.
[66] M. Pourbaix, Atlas of Electrochemical Equilibria in Aqueous Solutions, National Association of Corrosion Engineers, 1974.
[67] J. Hesketh, Q. Meng, D. Dowson, A. Neville, Biotribocorrosion of metal-on-metal hip replacements: how surface degradation can influence metal ion formation, Tribol. Int. 65 (2013) 128–137.
[68] D.O. Halwani, P.G. Anderson, J.E. Lemons, W.D. Jordan, A.S. Anayiotos, B.C. Brott, In-vivo corrosion and local release of metallic ions from vascular stents into surrounding tissue, J. Invasive Cardiol. 22 (11) (2010) 528–535.
[69] D.J. Langton, S.S. Jameson, T.J. Joyce, N.J. Hallab, S. Natu, A.V.F. Nargol, Early failure of metal-on-metal bearings in hip resurfacing and large-diameter total hip replacement A CONSEQUENCE OF EXCESS WEAR, J. Bone Joint Surg.-Br. Volume 92B (1) (2010) 38–46.